

Assignment 1

BEM Wind Turbine

Carlos Espinós Garcia
Niklas Perujo
Bernat Serra Zueras

Rotor and Wake Aerodynamics



Contents

1	Introduction	1
1.1	Assignment BEM BERNAT	1
1.2	Single polar innacuracies	1
2	Blade Element Momentum theory	3
2.1	Main assumptions of the BEM theory NIKLAS	3
2.1.1	Assumptions	3
2.1.2	Corrections	3
2.2	Code flow chart CARLOS	3
3	Results	5
3.1	BEM aligned rotor	5
3.1.1	Main outputs	5
3.2	BEM yawed rotor NIKLAS	9
3.2.1	Main outputs NIKLAS	10
3.2.2	Influence of numerical discretization	14
3.3	Influence of the tip correction CARLOS	16
3.4	Evaluation of stagnation enthalpy CARLOS	17
3.5	System of circulation and vorticity CARLOS	20
3.6	Operational point NIKLAS	23
4	Optional	25
4.1	Explanation of the design approach used for maximizing the Cp or efficiency	25
4.2	Plots with explanation of the new designs.	25
5	Conclusions NIKLAS	27
	Bibliography	29

Introduction

1.1. Assignment BEM BERNAT

This group assignment is based on the study of a Wind Turbine rotor's performance. The methodology implemented is the Blade Element Moment theory. The BEM theory is a powerful procedure to use to compute the main flow characteristics in a quick and cheap process if compared to other alternatives such as CFD. This is one of the main reasons why the BEM is a widely used tool to estimate the rotor performance in the Wind Energy business.

This is an introductory study and therefore has some simplifications in the model.

1.2. Single polar inaccuracies

This study would have some inaccuracies as it is planned if it is compared to a modern commercial wind turbine. One of the most relevant inaccuracies is the fact that the aerodynamics coefficients in all the radial sections of the blade have been extracted from the same polar curve.

Firstly, using single polar means assuming that all the radial positions are operating at the same Reynolds number. This is most probably false. Because from the Reynolds definition:

$$Re = \frac{\rho \cdot W \cdot c}{\mu_{visc}} \quad (1.1)$$

It has to be considered that as a first approximation that the relative velocity perceived by the airfoil at each section is depending on the radius. The relative velocity can be estimated like:

$$W = \sqrt{(U_{\infty} \cdot (1 - a))^2 + (\Omega \cdot r(1 + a'))^2} \quad (1.2)$$

While the chord distribution is ruled by the equation:

$$c = 3 \cdot (1 - \mu) + 1 \quad (1.3)$$

Then the Reynolds can be expressed as:

$$Re \quad Re(\mu) = \frac{\sqrt{(U_{\infty} \cdot (1 - a))^2 + (\lambda \cdot U_{\infty} \cdot \mu \cdot (1 + a'))^2} \cdot c(\mu)}{\nu} [-] \quad (1.4)$$

Then, as an example it is extracted the maximum and minimum Reynolds values from a BEM calculation at TSR = 8 with the converged inductions for the velocity. These sections would have a chord

$$\text{Blade root chord} \quad c(0.208) = 3 \cdot (1 - 0.208) + 1 = 3.376 \text{ m} \quad (1.5)$$

$$\text{Blade tip chord} \quad c(0.672) = 3 \cdot (1 - 0.672) + 1 = 1.984 \text{ m} \quad (1.6)$$

While the Reynolds would be.

$$\text{Blade root Re } Re(0.208) = \frac{\sqrt{(10 * (1 - a))^2 + (8 \cdot 10 \cdot 0.208 \cdot (1 + a'))^2} \cdot c(0.208)}{v} = 4.47 \cdot 10^6 \quad (1.7)$$

$$\text{Blade maximum Re } Re(0.672) = \frac{\sqrt{(10 * (1 - a))^2 + (8 \cdot 10 \cdot 0.672 \cdot (1 + a'))^2} \cdot c(0.672)}{v} = 7.63 \cdot 10^6 \quad (1.8)$$

Usually the increase in relative velocity along the blade is higher than the decrease in chord. Hence, the Reynolds number will be larger close to the tip, which usually means improving the aerodynamic coefficients performance.

Secondly, there are several models proposed as the one written by Snel et al. making reference to correction model of the polar data caused by the 3D effects. In particular, the one proposed by Snel states that it appears a delay in the stall of the sections closer to the root where the relative velocity is smaller. The Snel correction is modeled like eq (1 3.190) in the Wind Energy Handbook.

$$C_{L_{3D}} = C_{L_{2D}} + 3 \cdot \left(\frac{c}{r}\right)^2 \cdot \Delta C_L \quad (1.9)$$

This was initially pointed out by Himmelskamp, who observed in propellers *"lift coefficients being attained at the inboard section of a rotating blade which are significantly in excess of the maximum value possible in two-dimensional static tests."* These effects could have been taken into account in this study by using different airfoil polars depending on the blade section. Alternatively, it is also possible to include the 3D correction equations to the BEM code when extracting the aerodynamics coefficient from the polar files.

And lastly, it is not an strict inaccuracy, but nowadays wind trubine designs tend to optimize the structural and aerodynamics performance of a rotor. And to achieve that goal it is common to use different airfoils along the blade, which would yield different polar curves, as opposed to this study. Therefore it would be closer to the optimal to use slender airfoils near the tip to maximixe the aerodynamic performance and thicker airfoils closer to the root in order to increase their stiffness and load-carrying capacity.

2

Blade Element Momentum theory

2.1. Main assumptions of the BEM theory NIKLAS

2.1.1. Assumptions

The Blade Element Method is a combination of blade element theory and momentum theory to calculate the induced velocity at the rotor. Blade element theory is used to break down the blade into smaller parts and determine the forces acting on the blade element as it makes a revolution. These forces are added up to determine the forces acting on the whole rotor. Momentum theory helps to calculate the induced velocity at the rotor. The main assumption of BEM theory is that the force created by a blade element is solely responsible for the change of momentum of the air which passes through the annulus swept by the element [1]. This means that there is no radial interaction between the flows through different annuli, which can only be true if the axial flow induction does not vary radially [1]. This assumption is not correct but is acceptable [1].

2.1.2. Corrections

This assumption imposes some limitations on the model which are overcome through several corrections. Firstly, at high axial induction values, a , pure BEM theory predicts flow reversal in the wake. In reality the wake becomes turbulent and mixes with the free stream air. This mixing cannot be captured by BEM theory and so a correction is used. The correction used here is the Glauert correction for heavily loaded rotors further explained in section 2.2. Another limitation of BEM is that it assumes a uniform loading over the rotor which is not true when the rotor has a finite number of blades. A finite number of blades leads to a concentration of loading on the blades and each blade sheds vortices at the tip and root. These vortices cause an increase in axial induction at the edges of the blade which can be modeled with Prandtl's tip corrections which is further explored in section 3.3.

2.2. Code flow chart CARLOS

The code structure for solving the BEM equations in one cell at a given azimuth and radius is explained below.

1. First guess for the flow induction factors: $a_0 = 1/3$ and $a'_0 = 0$.
2. Forces estimation.
 - (a) The local velocities at the given azimuth and radius are calculated.
 - i. The yaw flow correction constant is estimated: $\chi = (0.6a + 1)\gamma$ and $K = 2 \tan 1/2\chi$.
 - ii. Axial velocity: $u_a = \cos \gamma - a(1 + K\mu \sin \psi)$.
 - iii. Tangential velocity: $u_t = \lambda\mu(1 + a') - \sin \gamma \cos \psi$.
 - (b) Flow angle determination from the local velocities: $\tan \phi = u_a/u_t$.
 - (c) Angle of attack is determined from the flow angle ϕ and blade geometry: $\alpha = \phi - \beta$.

- (d) Aerodynamic coefficients c_l and c_d are obtained from airfoil polar curve.
 - (e) The forces are estimated using the Blade Element Theory.
 - i. Axial force: $F_x = 1/2(u_a^2 + u_t^2)(c_l \cos \phi + c_d \sin \phi)cB\Delta\phi/2\pi$.
 - ii. Tangential force: $F_t = 1/2(u_a^2 + u_t^2)(c_l \sin \phi - c_d \cos \phi)cB\Delta\psi/2\pi$.
3. Induction factors estimation.
- (a) Cell surface: $dS = r\Delta r\Delta\psi$.
 - (b) Prandtl's loss factor: $f(\mu) = 2/\pi \arccos \left[\exp \left(-B/2 ((1 - \mu)/\mu) \sqrt{1 + (\lambda^2 \mu^2)/((1 - a)^2)} \right) \right]$.
 - (c) Axial induction factor.
 - i. Thrust coefficient: $C_T = F_x/(1/2u_\infty^2 \Delta S)$.
 - ii. Thrust coefficient limit for applying Glauert correction for heavily loaded rotors: $C_{T_2} = 2\sqrt{C_{T_1}} - C_{T_1}$, where $C_{T_1} = 1.816$.
 - iii. If $C_T < C_{T_2}$, $a = 1/2 - 1/2\sqrt{1 - C_T}$.
 - iv. If $C_T \geq C_{T_2}$, $a = 1 + (C_T - C_{T_1})/(4\sqrt{C_{T_1}} - 4)$.
 - (d) Tangential induction factor.
 - i. Tangential force coefficient: $C_{F_t} = F_t/(1/2u_\infty^2 \Delta S)$.
 - ii. Tangential induction factor: $a' = C_{F_t}/(4a(1 - a)\lambda\mu)$.
 - (e) Correct the flow induction factors with Prandtl's loss factor: $a = a/f$ and $a' = a'/f$.
4. Convergence check.
- (a) Estimate the error: $e = \max(|a - a_0|, |a' - a'_0|)$.
 - (b) If the error is larger than the tolerance, the process is repeated from step 2 with $a_0 = 0.75a_0 + 0.25a$ and $a'_0 = 0.75a'_0 + 0.25a'$.
 - (c) If the error is smaller than the tolerance, the calculation has converged.

3

Results

In this section are presented the main outcomes obtained when simulating the wind turbine model described previously. First are presented the results estimated for a wind turbine rotor that is aligned with the incoming flow. Next are presented the same results but for a rotor that it is not laterally aligned with the incoming flow, named as yawed rotor. After that its is described the effect of some extra features included in the BEM analysis such as the influence of the tip correction and numerical discretization, the evaluation of stagnation enthalpy or the evaluation of the system's circulation and vorticity.

Describe the initial conditions, table, cool

3.1. BEM aligned rotor

In this section it is considered that the rotor is fully aligned with the incoming flow as it would be in an ideal case. The discretization used to compute the main results includes 50 divisions in the radial position. The discretization is uniformly spaced using the same increment between adjacent sections.

3.1.1. Main outputs

The main outputs described in this sections would help the user identify the behaviour of the key variables that affect the rotor performance. Under this conditions the variables will only see its values affected by the radial position and not by their azimuthal position. The results are easily represented using only one value (the weighted average) per span section in a 2D plot that represents the variable versus the span section.

Angle of attack and inflow angle **BERNAT**

In Fig. 3.1 are displayed the inflow angle and angle of attack of each tip speed ratio study case.

The results are coherent with the tip speed ratio definition. In the study the freeflow incoming velocity is fixed at 10 m/s, so for the different TSR values the parameter changing is the rotor rotational speed Ω . At higher Ω values the rotational speed component is bigger and thus the inflow angle will decrease as shown in the plots. The angle of attack distribution also matches. Per definition, the geometrical twist of the blade could be obtained from these plots as the difference between the inflow angle and the angle of attack, which is a function of the μ parameter.

It must be highlighted that for the TSR=6 the inboard part of the blade is under stall conditions, hence will be a poor power generation section. This can be concluded because the stall AoA is included in the plot. In this study the stall AoA has a constant value along the entire span because the blade is built entirely with the same airfoil model. In commercial WTGs the blades use different airfoils depending on the radial section. If this WT model had to be design to operate most of the time under these conditions the optimal aerodynamic performance would probably be given at a TSR between 6 and 8. Because as it can be seen from Fig XXX, the maximum CL/CD ratio is obtained at AoA ranged between 7.5 and 9.25 degrees.

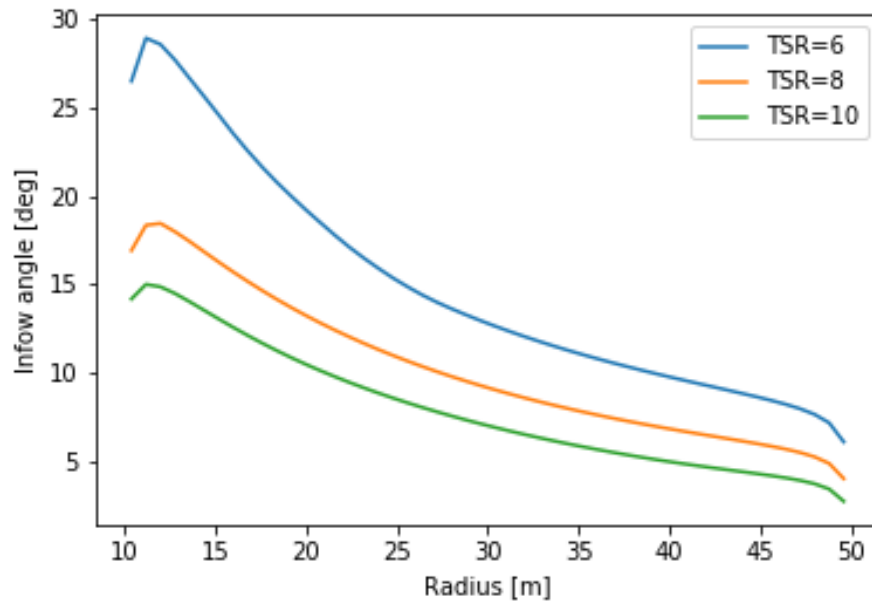


Figure 3.1: Inflow angle vs. Radius distribution at different TSR values

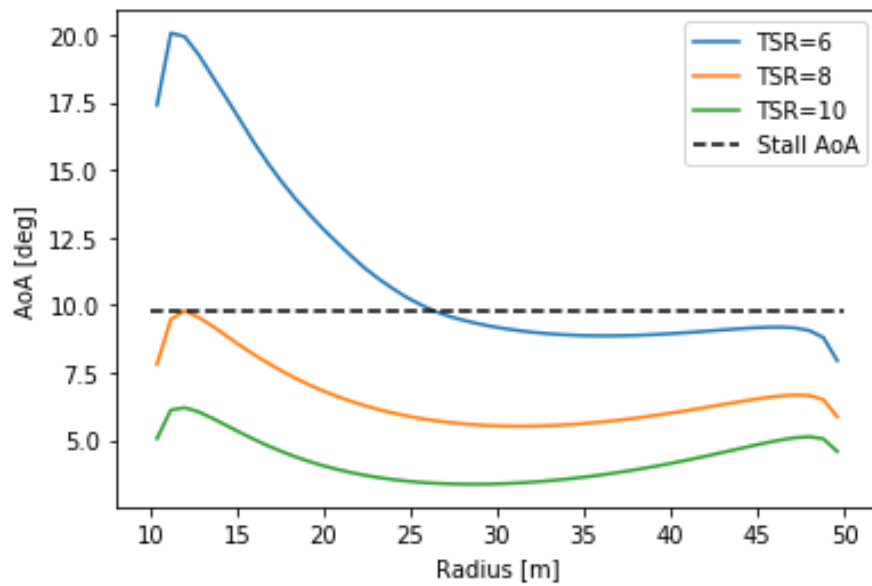


Figure 3.2: Angle of attack vs. Radius distribution at different TSR values

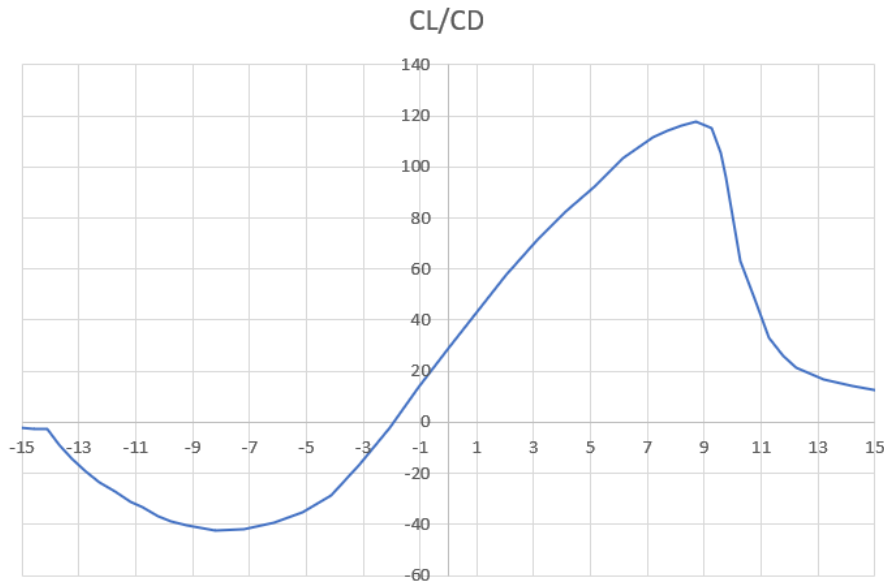


Figure 3.3: CL/CD ratio vs. Radius

Axial and azimuthal inductions **BERNAT**

In Fig. 3.1 are displayed the distribution of axial and tangential inductions of TSR case study.

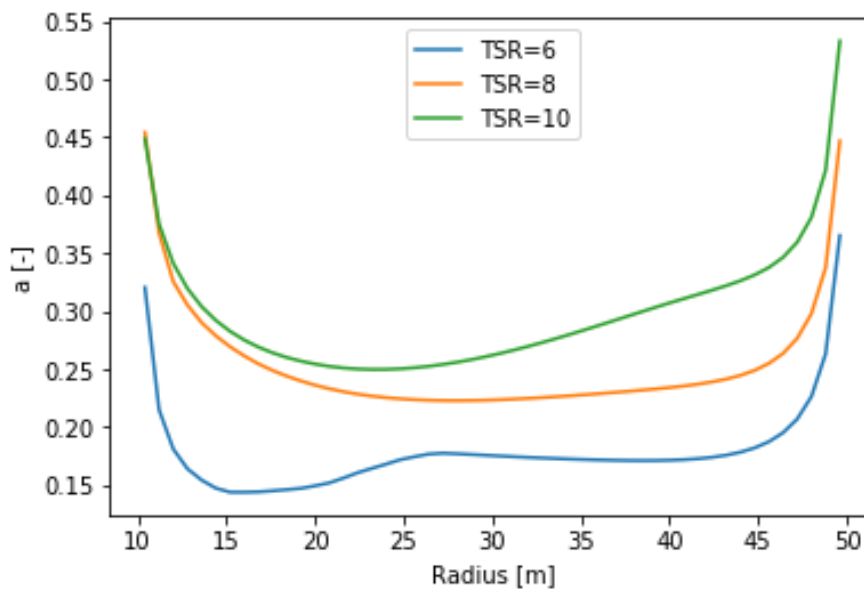


Figure 3.4: Axial induction factor vs. Radius distribution at different TSR values

Thrust and azimuthal loading **BERNAT**

In Fig. 3.6 are displayed the distribution of axial and tangential loads acting on the rotor for each TSR case study.

As it is mentioned in the previous subsection, in the TSR=6 operation regime the inboard part of the blade (approximately until 25m) loses its capacity to extract energy from the wind to generate thrust and torque. Under these conditions the inboard sections are experiencing inflow and AOA angles too high and the cross-sections airfoils are operating outside their optimal regime. This effect could have been partly mitigated if the polars of those inner sections would have been corrected by the 3D effects

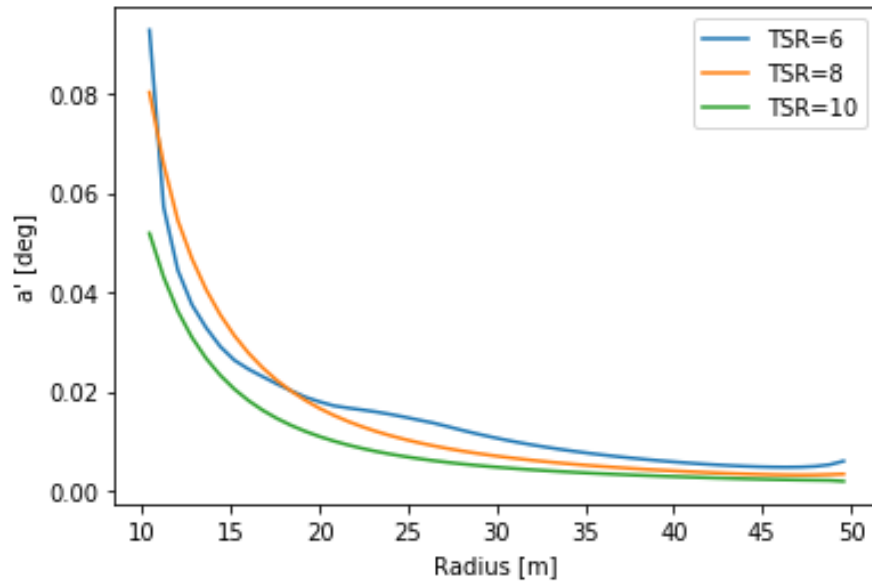


Figure 3.5: Tangential induction factor vs. Radius distribution at different TSR values

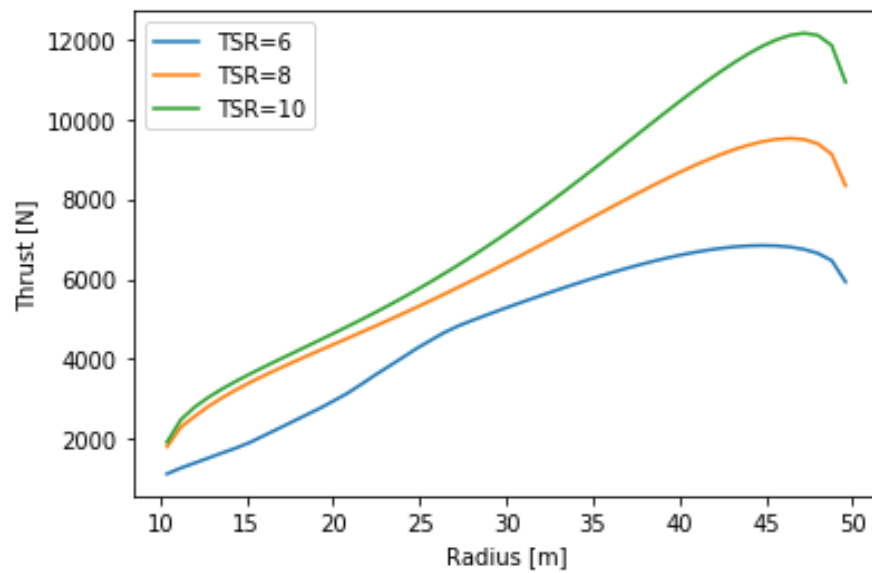


Figure 3.6: Thrust vs. Radius distribution at different TSR values

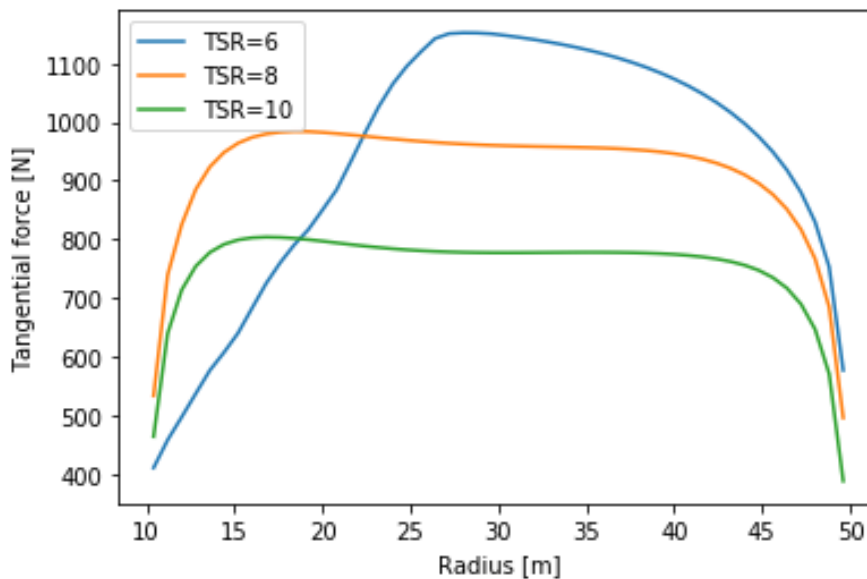


Figure 3.7: Tangential force vs. Radius distribution at different TSR values

such as the Snel correction proposed in the introduction.

The most intensively-loaded sections are the ones closer to the tip. This was expected by looking at the AoA radial distribution. Those sections operate at the upper range of the CL linear region, close to stall, where the CL/CD ratio is better. But the AoA is not the only parameter affecting the performance, if it was like that the curves at higher TSR would generate larger loads. It has to be taken into account that in the way the TSR modifications in this assignment consider the incoming flow velocity U_∞ and Blade Radius R constant, meaning that the only parameter changing its value is the rotor speed Ω . Thus, what is being done when increasing the TSR is increasing the absolute value of the relative velocity seen by the sections, which would end up increasing severely the loads as it affects the term that is at a power of 2.

Total thrust and torque BERNAT

Table ?? provides the values obtained for the total Thrust and Torque generated by the WTG at the different TSR. The total thrust force has been computed as the sum of the axial forces f_x generated by each annulus section. The total torque has been computed as the sum of the products of the tangential force f_y and the radial position r of each annular section. In the previous sections the loads have been provided without taking into account the density, thus with units $\frac{N}{kg/m^3}$. However, in Table XXX the total forces have been estimated for a standard density $\rho = 1.225 kg/m^3$ to give a better overview of the rotor performance.

	TSR = 6	TSR = 8	TSR = 10
Thrust [kN]	235.443	316.605	369.669
Torque [kN·m]	1464.494	1361.402	1116.159

3.2. BEM yawed rotor NIKLAS

The results in this section were obtained for the rotor operating with tip speeds $\lambda = 6, 8, 10$ and yaw values of $\psi = 15, 30$ degrees. The discretization used here is the same as in section 3.1, however, since for the yawed case variables are not constant over the azimuth the discretization also includes 4 equally spaced divisions over the azimuth.

3.2.1. Main outputs NIKLAS

The main outputs in this section would help the user identify how the key variables that affect rotor performance are changed by a yaw angle of the incoming flow. The variables will vary radially and azimuthally and are, unless otherwise specified, averaged over the azimuth to give 2D plots that show variation only over the span.

Angle of attack and inflow angle NIKLAS

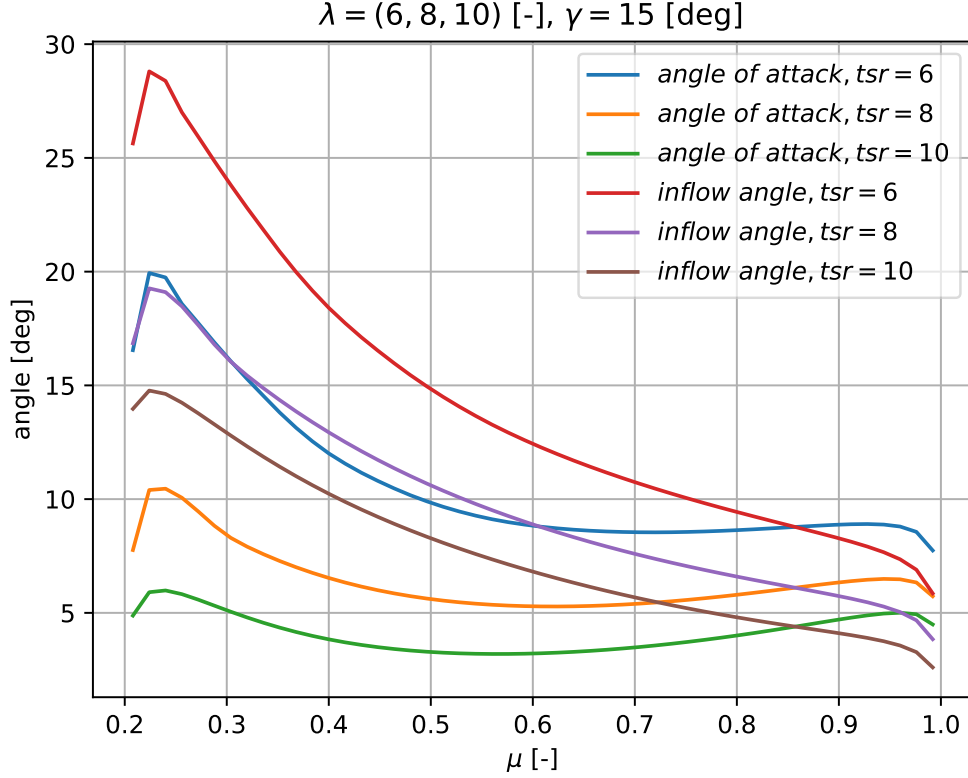


Figure 3.8: Angle of attack and inflow angle at a yaw of 15 degrees.

Figures 3.8 and 3.8 show the spanwise distribution of the angle of attack and inflow angle for TSR = 6, 8, 10 and for yaw angles of 15 and 30 degrees respectively. These plots are very similar in shape to the non-yawed case with the inflow angle decreasing with increasing radial direction and TSR. Since increasing TSR means increasing rotational speed the inflow angle decreases due to a larger rotational speed component. Similarly, since the rotational speed increases with increasing radial position the inflow angle also decreases closer to the tip of the blade. It is again apparent that for TSR=6 the inboard part of the blade is under stall conditions. It should also be noted that for increasing yaw angles both the angle of attack and the inflow angle decreased for all TSR. This means that for a higher yaw angle and TSR=6 less of the blade is under stall conditions.

Axial and azimuthal inductions NIKLAS

Figures 3.10 and 3.11 present the spanwise distribution of the axial and azimuthal inductions, a and a' . The shape of these plots is similar to the non-yawed case, however, the values for both axial and azimuthal inductions decrease with increasing yaw angle.

Thrust and azimuthal loading NIKLAS

Figures 3.12 and 3.13 present the spanwise distribution of the thrust and azimuthal loading on the blade. The shape of the plots again mirrors the non-yawed case except that the values decrease with increasing yaw. Note that the axial thrust increases with increasing TSR, while the azimuthal loading decreases with increasing TSR. It should also be noted that for TSR=6 the azimuthal loading near the root drops off. This is because for TSR=6 the blade near the root is under stall conditions.

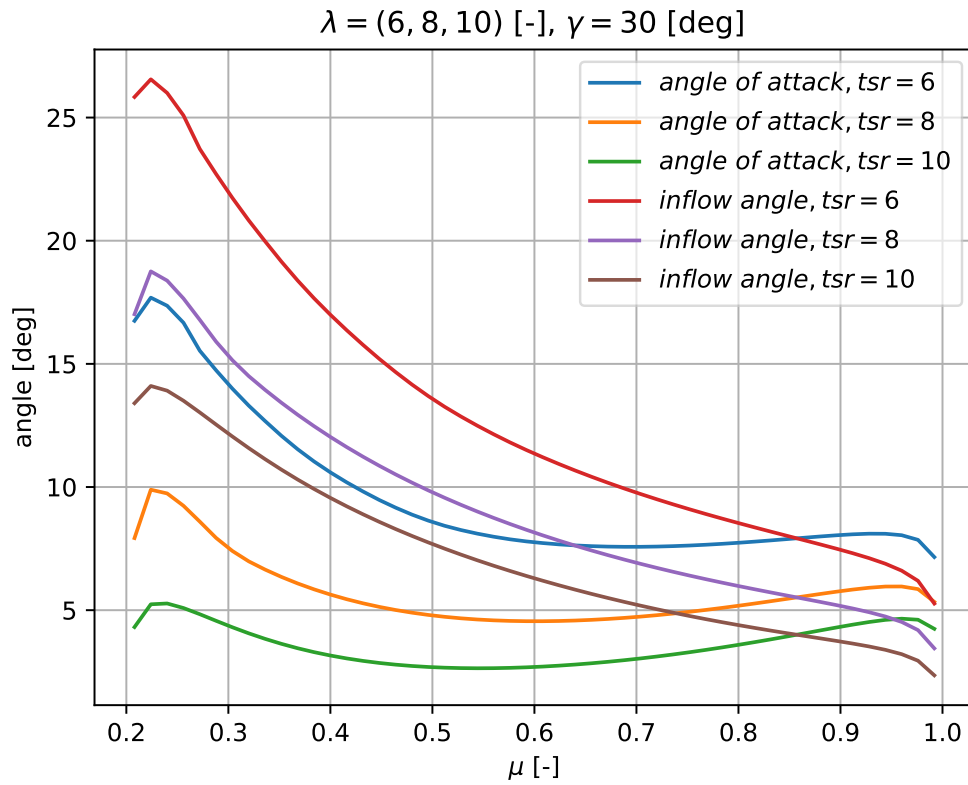


Figure 3.9: Angle of attack and inflow angle at a yaw of 30 degrees.

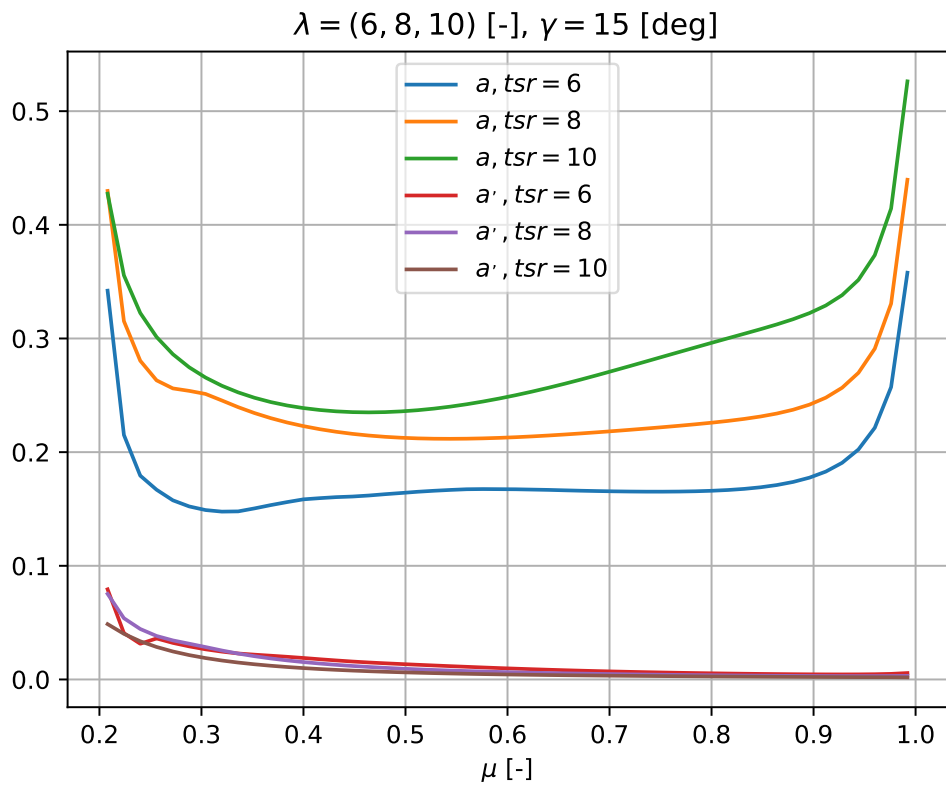


Figure 3.10: Axial and azimuthal inductions at yaw of 15 degrees.

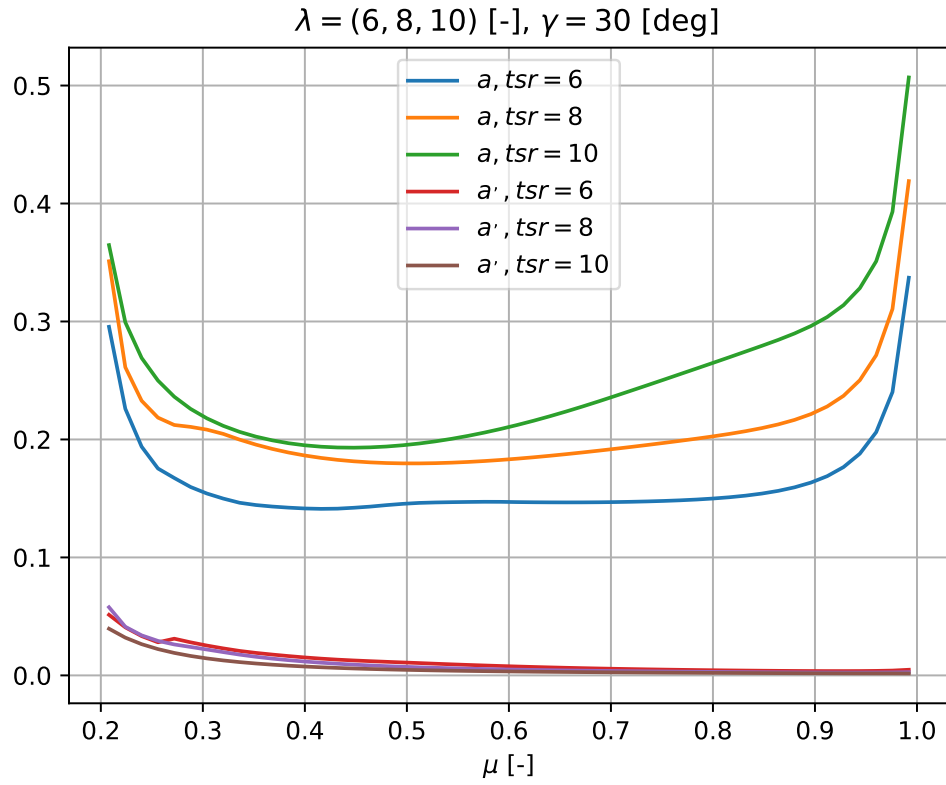


Figure 3.11: Axial and azimuthal inductions at yaw of 30 degrees.

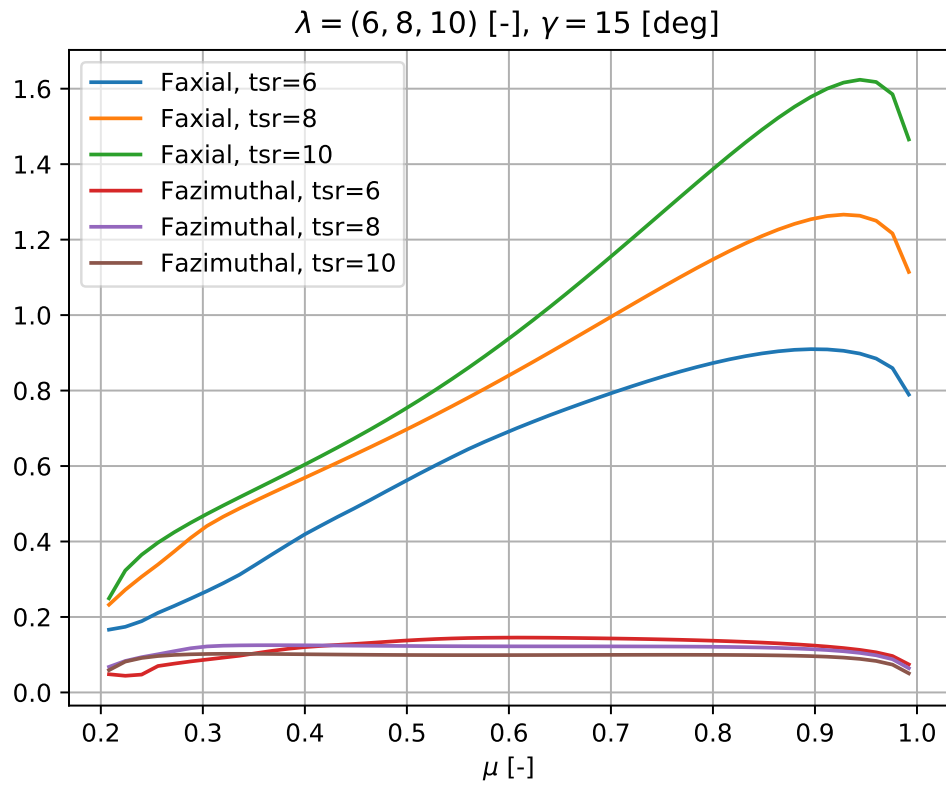


Figure 3.12: Thrust and azimuthal loading normalized by $\frac{1}{2} \rho U_{\infty}^2 R$.

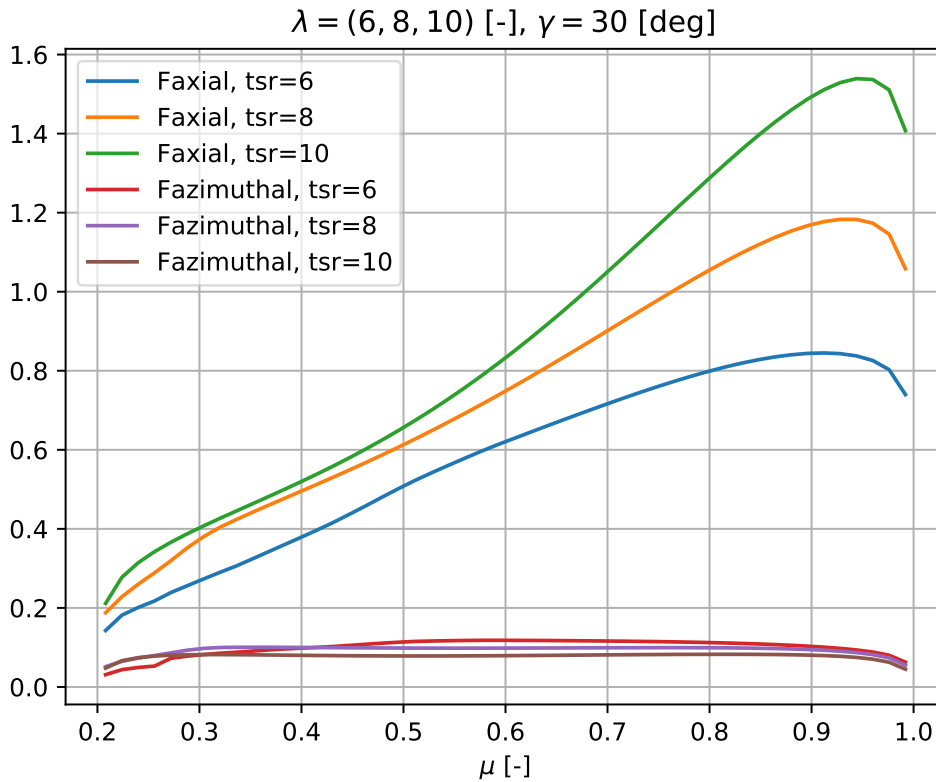


Figure 3.13: Thrust and azimuthal loading normalized by $\frac{1}{2}\rho U_\infty^2 R$.

Total thrust and torque NIKLAS

Tables 3.1 and 3.2 provide the values of the total thrust and torque generated by the wind turbine at TSR=6,8,10 and yaw angles 15 and 30 degrees respectively. The total thrust was computed by taking the average axial force over the azimuth of each annulus section and taking their sum. Similarly, the total torque was computed by taking the average tangential force over the azimuth of each annulus section and taking their sum. As in the non-yawed case these loads were calculated without density and so a standard density $\rho = 1.225 \text{ kg/m}^3$ was used.

Table 3.1: Thrust and Torque for yaw angle of 15 degrees.

	TSR=6	TSR=8	TSR=10
Thrust [kN]	230.370	305.932	359.225
Torque [kN*m]	1378.321	1273.163	1050.505

Table 3.2: Thrust and Torque for yaw angle of 30 degrees.

	TSR=6	TSR=8	TSR=10
Thrust [kN]	211.879	276.674	326.935
Torque [kN*m]	1137.425	1035.234	858.573

Azimuthal Variation NIKLAS

For the case of a yawed turbine the results are not constant over the azimuth. This variation is presented here in Fig. 3.14 for the axial induction for TSR=6 and a yaw of 15 degrees. The figure was computed using a discretization of 50 radial sections and 50 azimuthal sections. While there is some variation with the azimuth it is much less than the variation that occurs in the radial direction at the tip and root of the blades. This means that while the power extracted is reduced there are no significant extra loads on the blade to prevent operation. Thus it is sufficient to analyze the values averaged over the azimuth.

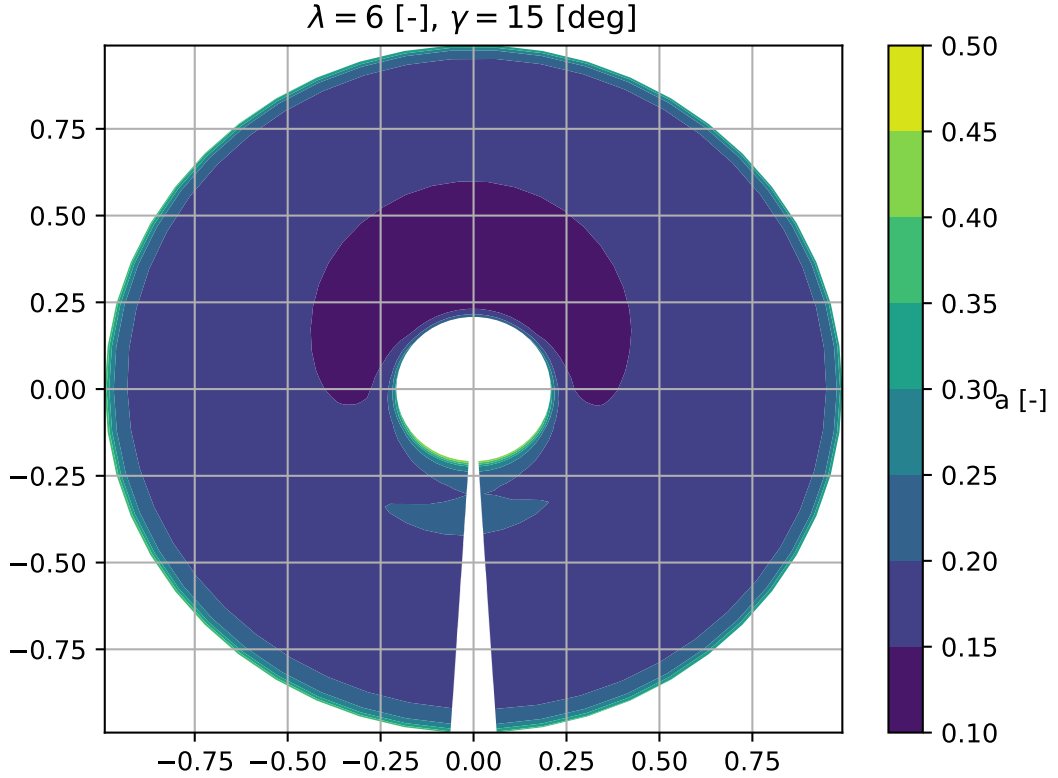


Figure 3.14: The azimuthal variation of the axial induction.

3.2.2. Influence of numerical discretization

This subsection provides information about the influence that the numerical discretization has in the final results. The rotor conditions taken to carry out this analysis are at fixed at $\text{TSR} = 8$ and $U_\infty = 10$ m/s. For the yawed cases the misalignment angle is set to 15 degrees.

The first analysis is focused on the effect of the different spacing methods to apply in the radial divisions. The most straight-forward is to use an uniformly spaced distribution that has a constant radius increment in adjacent sections. The proposed alternative in this study is to use a cosine-spaced radial distribution. This method is widely used for executing panel methods on 2D airfoils because an airfoil usually has more curvature on the LE. Hence, for more a more accurate calculation in this region it is necessary to have finer divisions. Figure XXX provides an example of how the distribution of μ nodes will be for a 15-nodes configuration using the two methods mentioned. The values in the y-axis are irrelevant, are just separated enough to provide a good overview of the x-axis discretization.

Taking into account Figure XXX it can be seen that the cosine spaced distribution provides smaller divisions at the edges of the range. For the WT model this would mean that the more refined regions in the study are in the root and tip of the rotor. Both regions have the feature to be the ones where the Prandtl tip correction factor has more effect and where it is also varying more with respect to the span. This is the main reason why it has been decided to use this kind of discretization here. The results for both methodologies are plotted in Figure 3.16. From this data it is obvious to conclude that the cosine spaced discretization is more efficient and converges faster. However it has to be mentioned that when forcing strict convergence tolerances the code has some trouble converging for more than 61 cosine-spaced divisions. This is probably due to the very tinny sections at the root and tip. Nevertheless, in the plot the value of Thrust for more than 61 divisions has been kept constant as it can be argued that the 60th value was the exact value, as it keeps the asymptotic trend showed by the uniformly spaced cases. So to reach the converged value with the uniform distribution it will be necessary to use around 100 sections, while for the cosine it is enough with 50, only the half of it. Thus, using the cosine space could save up to 50% of the computational effort.

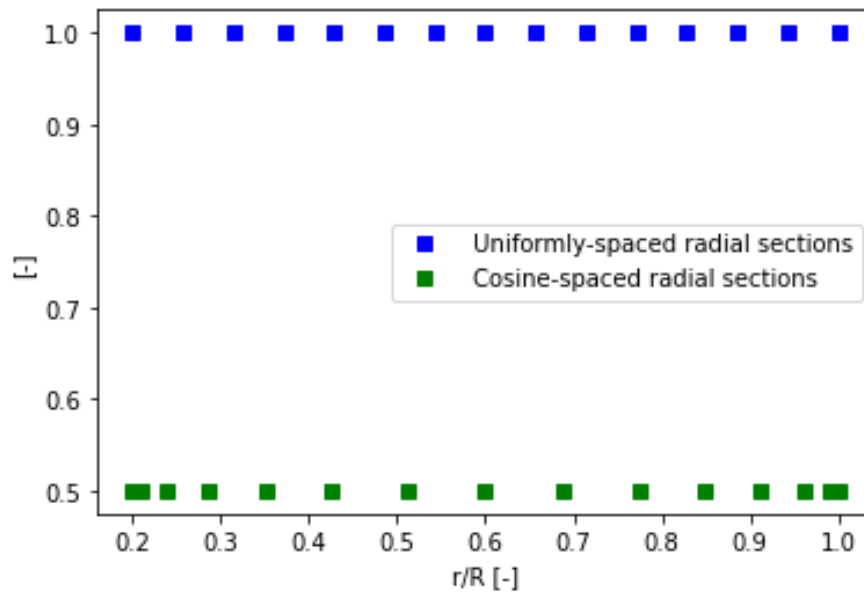


Figure 3.15: Distribution of 15 μ nodes with different division strategies

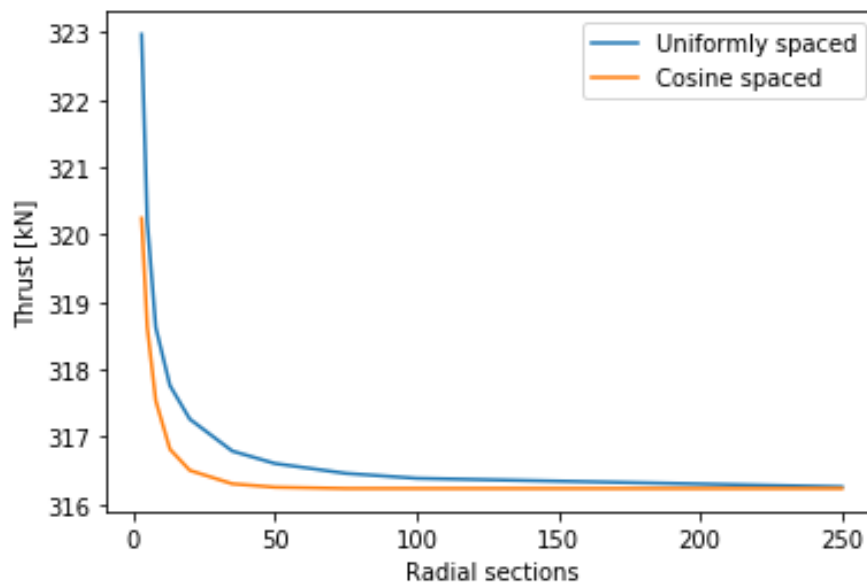


Figure 3.16: Total Thrust convergence vs. number of radial sections

Then a similar study has been carried out for the yawed case at 15 degrees and with 50 radial divisions for each method. Figure 3.17 displays the results obtained when using different numbers of azimuthal sections. Again, this study has been executed for the two radially spaced methods. In this case it can be seen that both methods do not converge in the same total Thrust value. This can be explained by looking again at Fig. 3.16. From this plot it can be extracted that at 50 radial sections, both methodologies had not yet reached the same value. This is the difference seen in Fig. 3.17. It is also worth to highlight that number of azimuthal sections convergence seems to be decoupled of the radial discretization methodology. Both techniques show variable behaviour until around 12 sections, where they reach a stable value. So computing the BEM in arcs of 30° seems to yield reliable results with this configuration.

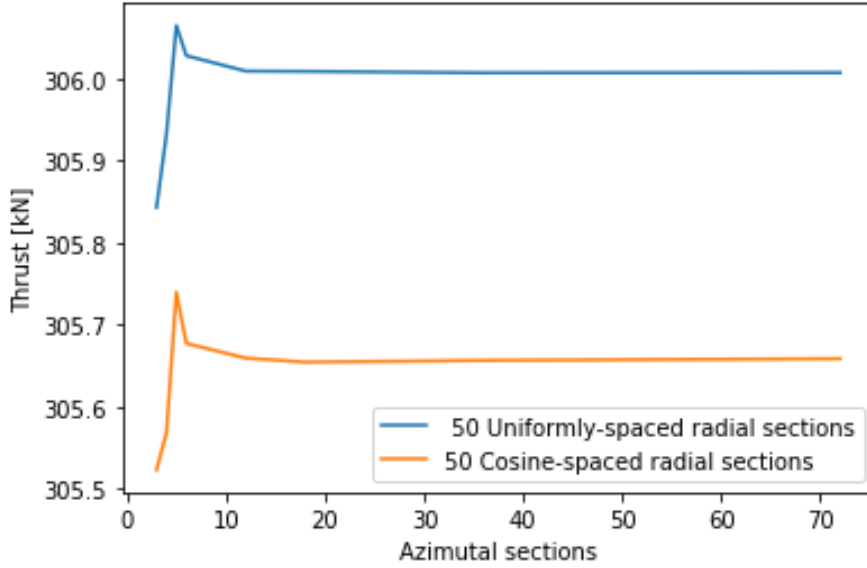


Figure 3.17: Total Thrust convergence vs. number of azimuthal sections

3.3. Influence of the tip correction **CARLOS**

The results shown in this section were obtained for the rotor described in the assignment instructions, operating with a tip speed ratio $\lambda = 8$ and no yaw. It can be seen that the tip correction reduces the power and thrust, resulting in a worse performance. Indeed, the rotor without the tip correction has a higher C_P/C_T ratio.

Near the blade tip, the flow angle ϕ is reduced due to the tip vortex (Figure 3.18), because it induces a larger axial velocity (Figure 3.20). Having a lower flow angle ϕ results in a reduced power extraction, which is proportional to $c_l \sin \phi - c_d \cos \phi$ (Figure 3.21) [1]. However, reducing the flow angle ϕ contributes to an increase of the thrust, since it is proportional to $c_l \cos \phi + c_d \sin \phi$.

Note that c_l also decreases due to the reduction of ϕ , because it implies a decrease of the angle of attack α (Figure 3.19). Moreover, the relative velocity, which also affects the loads, will also be larger for the case without tip correction.

The tip correction tries to account for this effect. The expression Prandtl derived for that factor is shown in equation 3.1. Its value over the blade is plotted in Figure 3.22. It relates the induction factor near the blade a_b with the azimuth average a : $a_b = a/f$ [1].

$$f(\mu) = \frac{2}{\pi} \arccos \left[\exp \left(-\frac{B}{2} \left(\frac{1-\mu}{\mu} \right) \sqrt{1 + \frac{\lambda^2 \mu^2}{(1-a)^2}} \right) \right] \quad (3.1)$$

- Power coefficient C_P
 - Tip correction: 0.4528

- No tip correction: 0.4757
- Increase: 5.05 %
- Thrust coefficient C_T
 - Tip correction: 0.6581
 - No tip correction: 0.6691
 - Increase: 1.67 %
- Power to thrust ratio C_P/C_T
 - Tip correction: 0.6880
 - No tip correction: 0.7109
 - Increase: 3.32 %

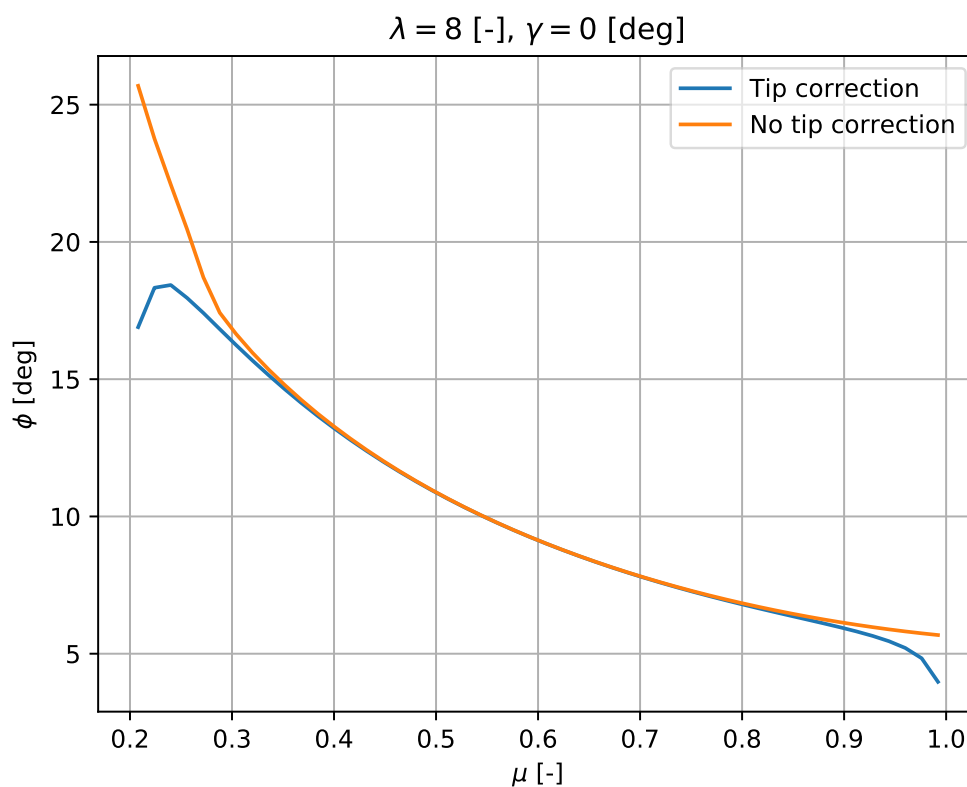


Figure 3.18: Flow angle distribution with and without tip correction.

3.4. Evaluation of stagnation enthalpy CARLOS

If heat exchange, viscous forces and compressibility effects are neglected, the flow temperature does not change. Therefore, it can be assumed that the air's internal energy is always constant. Then, the changes in stagnation enthalpy and stagnation pressure are equivalent. The mechanical energy equation (3.2) describes how the stagnation pressure p_t changes. Note that it has been obtained as the scalar product of the momentum equation and the velocity vector.

$$\vec{v} \cdot \vec{\nabla} p_t = \vec{v} \cdot \vec{\nabla} \cdot \vec{\tau} + \vec{v} \cdot \vec{f} \quad (3.2)$$

If viscous forces are not considered, $\tau = 0$, the stagnation pressure can only due to the body forces b work. The only domain region where these forces are not null, and therefore, exert some work is

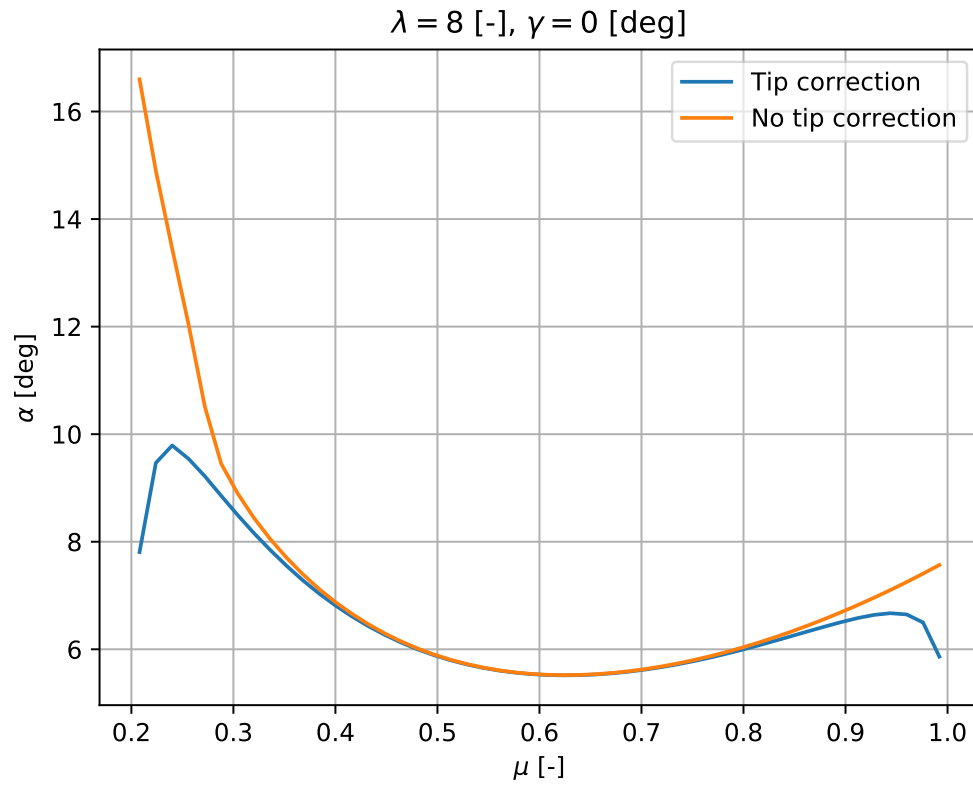


Figure 3.19: Angle of attack distribution with and without tip correction.

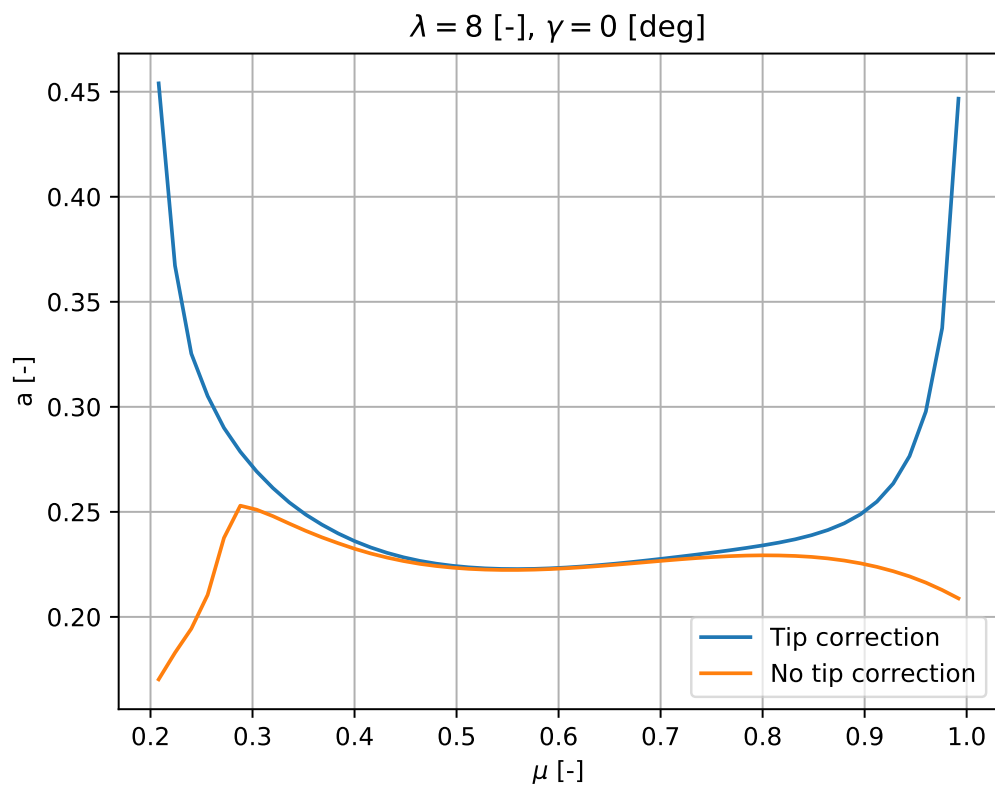


Figure 3.20: Axial induction distribution with and without tip correction.

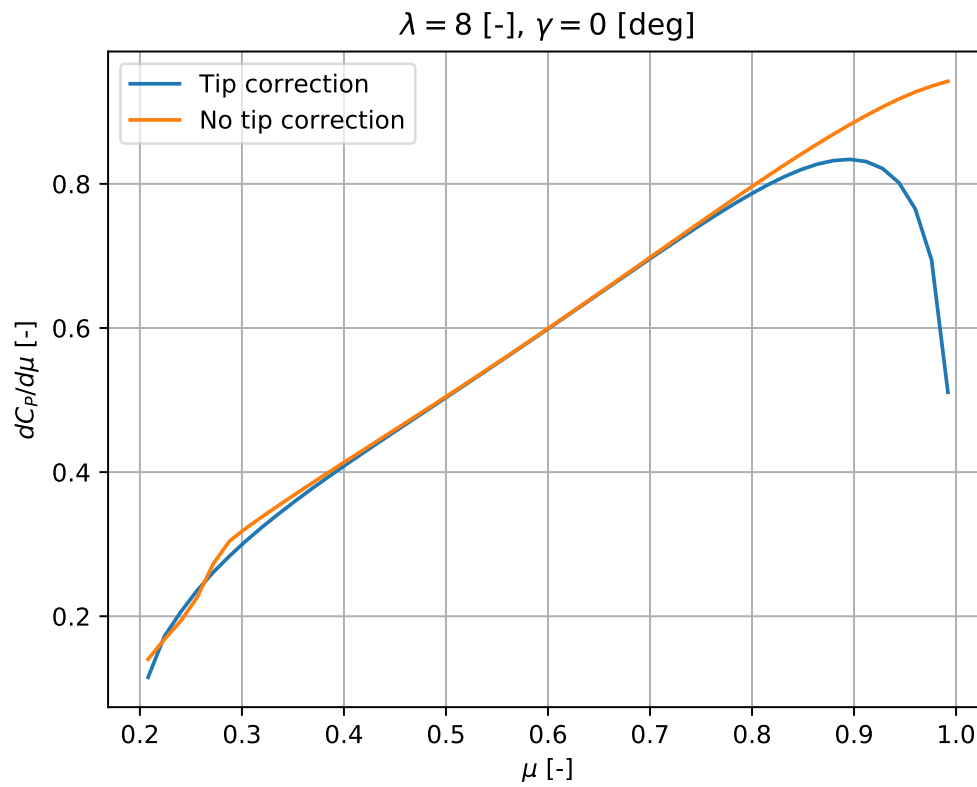


Figure 3.21: Power coefficient distribution with and without tip correction.

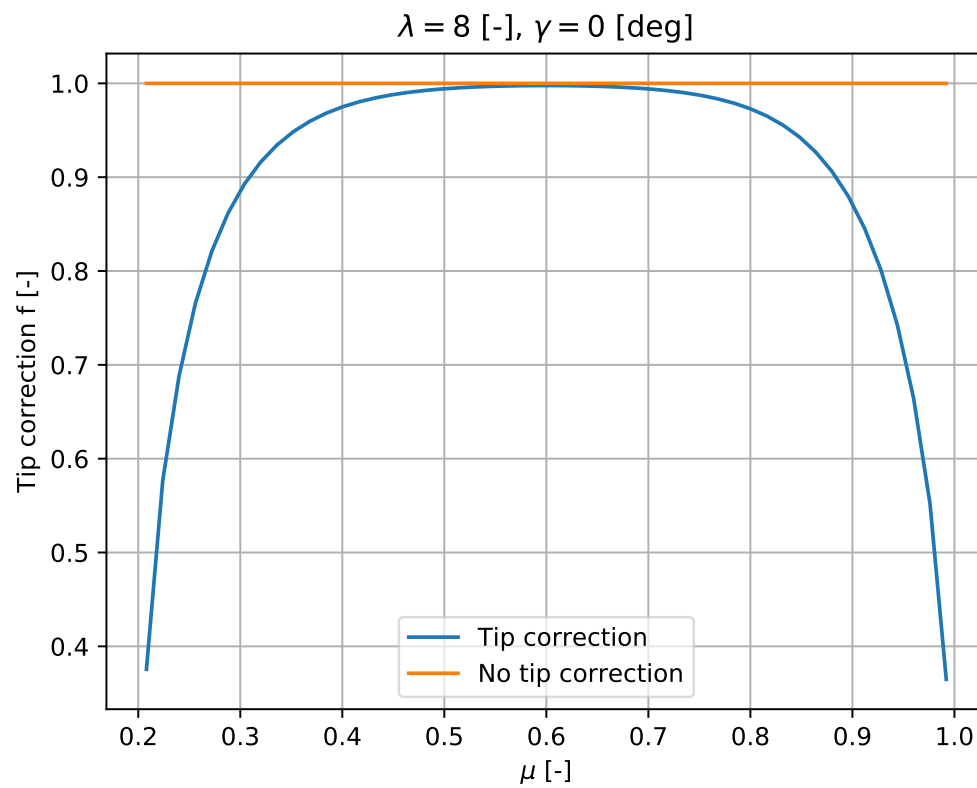


Figure 3.22: Prandtl's tip loss factor distribution with and without tip correction.

the rotor plane. This means that the stagnation pressure only changes across the rotor plane. See equations (3.3) and (3.4) for the stagnation pressure expressions up and down-stream of the rotor plane respectively. They are plotted in Figure 3.23.

$$p_{t_u} = p_a + \frac{1}{2} \rho u_\infty^2 \quad (3.3)$$

$$p_{t_d} = p_a + \frac{1}{2} \rho u_\infty^2 (1 - 2a)^2 \quad (3.4)$$

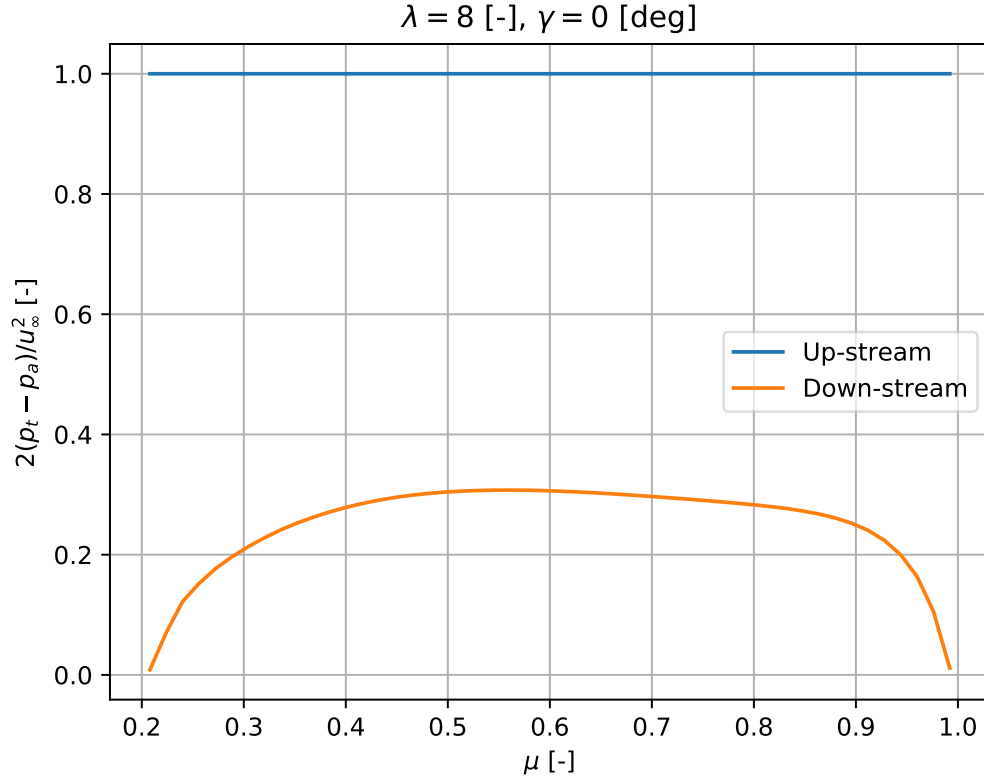


Figure 3.23: Stagnation enthalpy distribution.

3.5. System of circulation and vorticity **CARLOS**

The circulation distribution over the blade is shown in Figure 3.24. It has a more or less constant shape in the centre part of the blade, and vanishes quite steeply near the root and tip. This seems reasonable, since circulation is related to lift generation by the Kutta-Joukowski theorem: $l = \rho u_\infty \Gamma$. In the blade extremes, lift must be zero, since there is no surface that can create it.

The vorticity equation and Kutta-Jukowski theorem explain the changes observed in circulation. The thrust derivative with respect to the radius can be expressed using the Blade Element Theory, Kutta-Jukowski theorem and assuming no drag (3.5), or using the Momentum Theory (3.6).

$$\frac{dT}{dr} = l \cos \phi = \rho w \Gamma \cos \phi \quad (3.5)$$

$$\frac{dT}{dr} = \rho u_\infty (1 - a) u_\infty 2a 2\pi r \quad (3.6)$$

If the expressions (3.5) and (3.6) are equated, it can be seen that the circulation is related to the local thrust. This is shown in Figure 3.25, where the two sides of equation (3.7) are plotted. The slightly

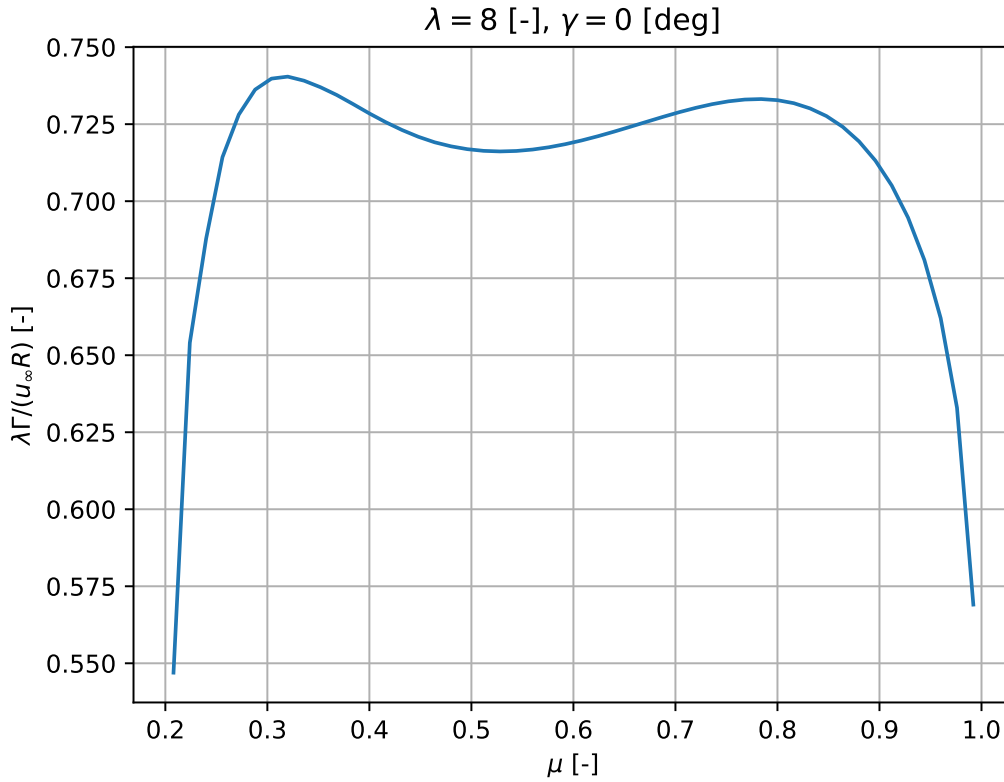


Figure 3.24: Circulation distribution.

higher values for the thrust coefficient may be due to the drag contribution, which is not accounted for in the circulation.

$$\frac{w\Gamma \cos \phi}{u_{\infty}^2 \pi r} = 4a(1-a) = C_T \quad (3.7)$$

Equation (3.7) is actually a different form of the vorticity equation (3.8).

$$\vec{v} \cdot \vec{\nabla} \vec{\omega} = \vec{\nabla} \times \vec{f} \quad (3.8)$$

Assuming there are no radial forces, and that vorticity only changes in its direction ($d\omega_i/dx_j = 0$, if $i \neq j$), the vorticity equation in the tangential direction can be simplified to better show how it relates to expression (3.7).

$$w \cos \pi \frac{d\omega}{r d\theta} = -\frac{df_x}{dr} \quad (3.9)$$

If equation (3.9) is integrated over the volume, expression 3.7 is obtained. Remark that $\int 1/r d\omega/d\theta dV = -\int \omega dS = -\Gamma$, and $\int df_x/dr dV = dT/dr$.

The same procedure can be done for the vorticity generation in the axial direction. In this case, the vorticity equation is the one shown in (3.10). The relationship between the circulation and tangential force is given by equation (3.11).

$$w \sin \pi \frac{d\omega}{dx} = \frac{df_{\theta}}{dr} \quad (3.10)$$

$$\frac{dS}{dr} = l \sin \phi = \rho w \sin \phi \Gamma = \rho u_{\infty} (1-a) \Omega r 2a' 2\pi r \quad (3.11)$$

The relationship between the tangential force and generation of circulation in the axial direction is depicted in Figure 3.26. The differences observed may be due to the drag, which reduces the tangential force created by the lift.

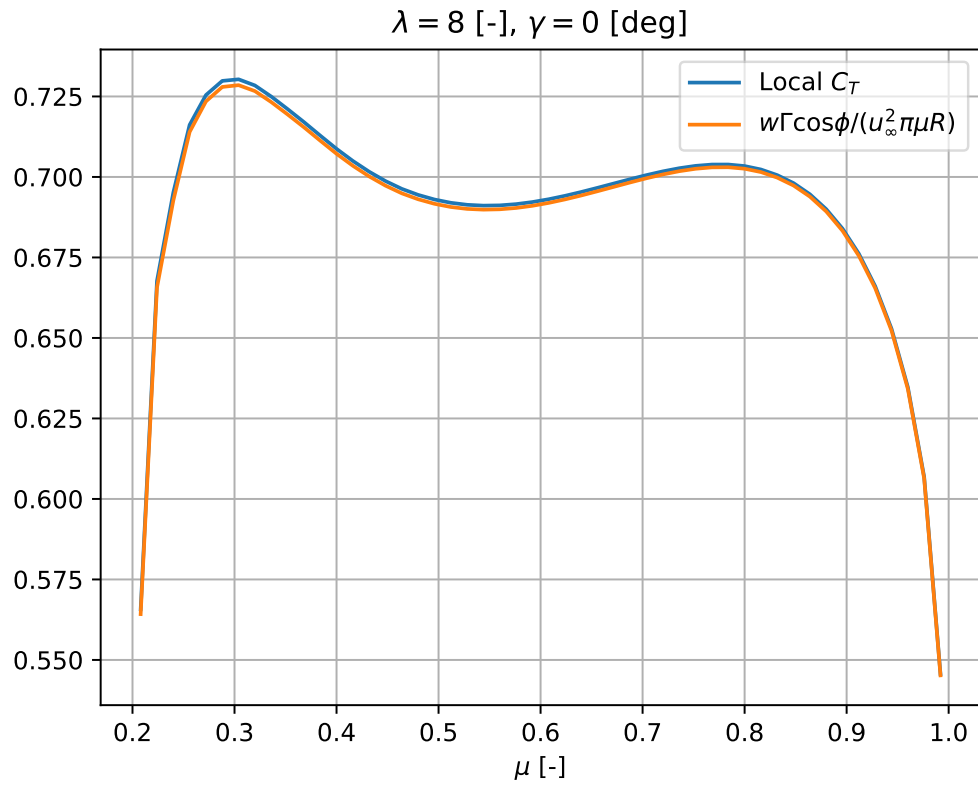


Figure 3.25: Circulation and local thrust coefficient distribution.

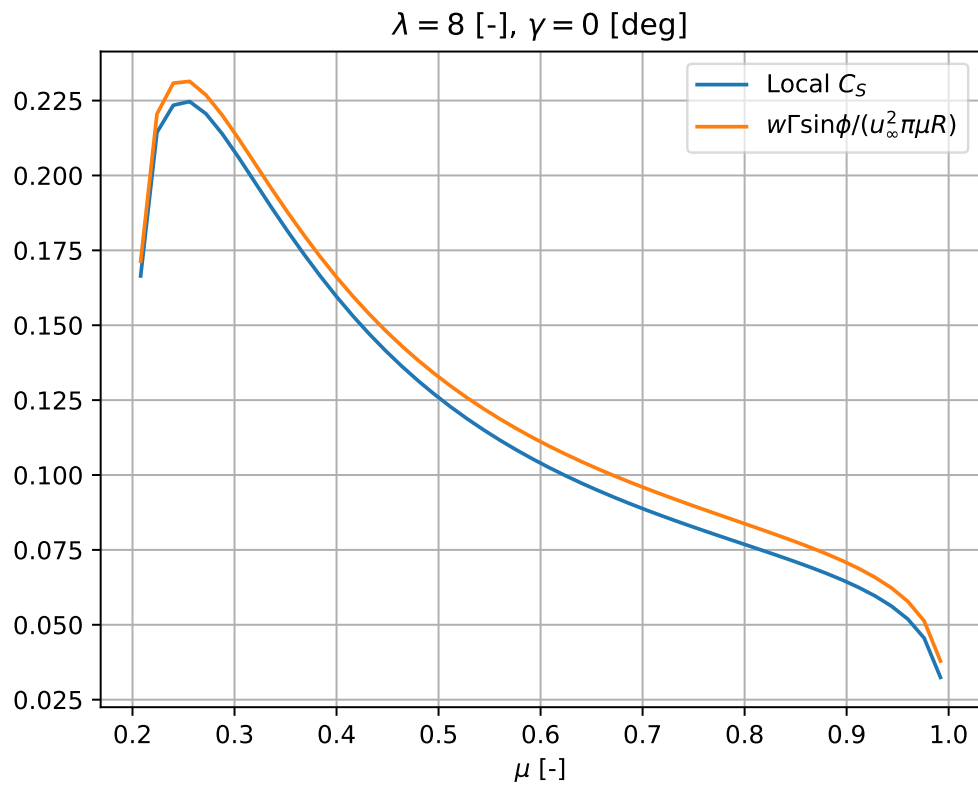
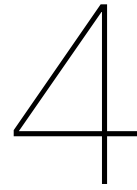


Figure 3.26: Circulation and local tangential coefficient distribution.

3.6. Operational point [NIKLAS](#)



Optional

4.1. Explanation of the design approach used for maximizing the Cp or efficiency

Blabla

4.2. Plots with explanation of the new designs

Rick Sanchez

5

Conclusions NIKLAS

SHORT discussion/conclusion, including the similarities and differences between the two rotor configurations (yaw vs. aligned rotor), flow field and operation

Bibliography

- [1] Burton, T. and Jenkins, J. and Sharpe, D. and Bossanyi, E. *Aerodynamics of Horizontal Axis Wind Turbines*, chapter 3, pages 39–136. John Wiley & Sons, Ltd, 2011. ISBN 9781119992714. doi: <https://doi.org/10.1002/9781119992714.ch3>. URL <https://onlinelibrary.wiley.com/doi/abs/10.1002/9781119992714.ch3>.